INTERFACE AND PROCESSING CIRCUIT DESIGN FOR IONIC LIQUID HYDROGEN SENSORS

by

SHUAISHUAI LING

A thesis submitted in partial fulfillment of the
requirements for the degree of

MASTER OF SCIENCE IN ELECTRICAL AND COMPUTER ENGINEERING

2025

Oakland University
Rochester, Michigan

Master Advisory Committee:

Hongwei Qu, Ph.D., Chair
Jia Li, Ph.D.
Amanpreet Kaur, Ph.D.

To the world

ACKNOWLEDGMENTS

I would like to express my deepest gratitude to my advisor, Prof. Hongwei Qu, for his invaluable guidance, encouragement, and support throughout the course of my graduate study and research. His insight and expertise have been essential to the completion of this work.

I am sincerely grateful to Prof. Xiangqun Zeng and her group at the University of Missouri for their collaboration and for providing experimental hydrogen concentration data, which greatly supported the validation of this system. I would also like to thank Prof. Yong Xu and his research group at Wayne State University for providing the electrochemical electrode chips that enabled experimental testing of the ionic-liquid hydrogen sensor. Their contributions were vital for this project.

I would also like to acknowledge my thesis committee members, Prof. Jia Li and Prof. Amanpreet Kaur, for their valuable feedback and constructive suggestions that helped improve this thesis.

Finally, I would like to thank my family and friends for their unconditional support, encouragement, and patience throughout my graduate studies.

Shuaishuai Ling

ABSTRACT

INTERFACE AND PROCESSING CIRCUIT DESIGN FOR IONIC LIQUID HYDROGEN SENSORS

by

Shuaishuai Ling

Adviser: Hongwei Qu, Ph.D.

Hydrogen detection is essential for fuel-cell safety, hydrogen storage, and leak prevention. Ionic-liquid electrochemical sensors generate ultra-low currents (pA–nA), requiring highly sensitive acquisition. This thesis work developed a precision analog front end featuring a potentiostat for stable electrode bias and a transimpedance amplifier with selectable feedback up to 1 GΩ for reliable current-to-voltage conversion. Input biasing and low-pass filtering improve stability and noise suppression. Although designed for IL-based H_2 sensors, the system is adaptable to other platforms requiring pico- to nano-amp current measurement.

A 32-bit delta-sigma ADC (ADS1262) digitizes signals with ultra-low noise, while integrated temperature, humidity, and pressure sensors enable environmental compensation. A low-power TI CC2640R2F SoC manages data processing and BLE communication. Experimental results demonstrate 50 pA-level resolution and $<0.5\%$ measurement error, with excellent linearity and stable wireless performance, supporting compact and portable next-generation electrochemical sensing systems.

TABLE OF CONTENTS

LIST OF TABLES

LIST OF FIGURES

LIST OF ABBREVIATIONS

ADC Analog-to-Digital Converter

CE Counter Electrode

DAC Digital-to-Analog Converter

GBW Gain Bandwidth Product

I^2C Inter-Integrated Circuit

IL H_2 sensor Ionic-Liquid Hydrogen Sensor

LDO Low-Dropout Regulator

MCU Microcontroller Unit

MEMS Micro-Electro-Mechanical Systems

OLED Organic Light-Emitting Diode

OP Amp Operational Amplifier

PCB Printed Circuit Board

PSRR Power Supply Rejection Ratio

RE Reference Electrode

RMS Root Mean Square

SD Secure Digital (memory card)

SMU Source Measure Unit

SNR Signal-to-Noise Ratio

SPI Serial Peripheral Interface

SPR Surface Plasmon Resonance

TIA Transimpedance Amplifier

WE Working Electrode

CHAPTER ONE

INTRODUCTION

1.1 Background

With the rapid development of the hydrogen economy, hydrogen has emerged as a key energy vector due to its high gravimetric energy density, zero-carbon combustion, and potential integration with renewable energy systems [1]. Hydrogen fuel cells, storage facilities, and industrial hydrogen applications are expected to play a crucial role in achieving carbon neutrality targets worldwide [2, 3]. However, hydrogen is colorless, odorless, and highly flammable [4]. Even trace leaks can cause severe safety hazards, highlighting the urgent need for reliable, sensitive, and portable hydrogen detection systems [5, 6].

Over the past decades, a variety of hydrogen sensing technologies have been proposed and developed, which can be broadly classified into four categories: semiconductor-type sensors, catalytic combustion sensors, optical fiber sensors, and electrochemical sensors [2, 5]. Each of these sensing approaches has unique advantages and limitations:

- **Semiconductor-type sensors:** Based on metal-oxide semiconductors (MOS) such as SnO_2 or ZnO, these sensors detect hydrogen through changes in surface conductivity [5, 7]. They offer low cost and simple structure, but they typically require high operating temperatures (200–400°C), leading to high power consumption and reduced long-term stability.

- **Catalytic combustion sensors:** These sensors oxidize hydrogen on a catalytic surface and measure the resulting change in thermal conductivity or resistance.

While they provide relatively fast response times, their selectivity is poor, cross-sensitivity to other flammable gases is significant, and their power consumption is also relatively high [2, 5].

- **Optical fiber sensors:** Utilizing techniques such as Surface Plasmon Resonance (SPR) or Bragg gratings coated with Pd-based films, optical fiber sensors can achieve high sensitivity and immunity to electromagnetic interference. However, their high cost, fragile structure, and limited suitability for portable integration hinder their large-scale deployment [6, 8].

- **Electrochemical sensors:** These sensors operate at room temperature and generate an electrical current proportional to the hydrogen concentration through electrochemical reactions. They feature high sensitivity, low power consumption, and good selectivity. Electrochemical sensors are therefore promising candidates for portable hydrogen detection devices [2, 9, 10].

Among electrochemical sensors, the recently developed Ionic-Liquid Hydrogen Sensor (IL H_2 sensor) has attracted significant attention. Unlike traditional aqueous systems that rely on dissolved redox mediators, the IL H_2 sensor utilizes noble-metal electrodes (e.g., Pt or Pd) in an ionic liquid electrolyte, where hydrogen is directly oxidized at the catalyst surface according to:

$$H_2 \rightarrow 2H^+ + 2e^- \tag{1.1}$$

In the presence of hydrogen, dissociation and oxidation at the working electrode generate electrons that flow through the external circuit, producing a current proportional to hydrogen partial pressure. Compared with conventional electrochemical sensors, IL H_2 sensor provides excellent chemical stability, negligible evaporation, and compatibility with miniaturized chip platforms, making it ideal for long-term and portable hydrogen sensing applications [5, 7, 8, 10].

However, one major challenge remains: the output current of such sensors is extremely small, often in the nanoampere (nA) or even picoampere (pA) range. This ultra-low current signal is highly susceptible to thermal noise, bias instability, and Printed Circuit Board (PCB) leakage effects. As a result, the design of a dedicated and highly sensitive readout circuit is essential to ensure reliable signal acquisition [11–13].

1.2 Research Objectives

To address the above challenges, this thesis focuses on the design of a complete readout system for IL H_2 sensor, capable of accurate pico ampere sensing. The system integrates both the core analog signal chain and essential peripheral functionalities. Specifically, the objectives of this work are:

1. **Potentiostat and DAC-controlled bias:** Design and implementation of a potentiostat circuit driven by a Digital-to-Analog Converter (DAC), enabling flexible AC/DC excitation. The DAC output is controlled by an Microcontroller Unit (MCU) through three push buttons, where one button toggles between modes (AC frequency, AC amplitude, DC bias amplitude), and the other two buttons increase or decrease the selected parameter. This design provides versatility for both constant potential operation and dynamic electrochemical testing.

2. **Ultra-low current amplification and filtering:** Development of a low-noise Transimpedance Amplifier (TIA) with gigaohm-level feedback resistors, followed by a second-order low-pass filter to suppress high-frequency noise. This ensures faithful conversion of pA/nA current signals into measurable voltages [11].

3. **High-resolution digitization and embedded processing:** Integration of a delta-sigma Analog-to-Digital Converter (ADC) with a low-power MCU to achieve accurate digital representation of the signals. The MCU handles data acquisition, DAC control, and system coordination.

4. **Peripheral modules and system robustness:** Incorporation of a BME280 sensor for environmental compensation, power management circuits (boost converters, Low-Dropout Regulator (LDO) regulators), and user interfaces including Organic Light-Emitting Diode (OLED) display and data storage. These modules ensure the system operates reliably under real-world conditions.

5. **System integration and validation:** Realization of the entire readout system on PCB, simulation-based performance analysis, and experimental validation using standard instruments (e.g., Keithley Source Measure Unit (SMU)) and hydrogen exposure tests.

1.3 Thesis Organization

The remainder of this thesis is organized as follows:

- Chapter 2 introduces the IL H_2 sensor and analyzes the system requirements for reliable readout.

- Chapter 3 presents the design of the core readout circuit, including the potentiostat, DAC, TIA, low-pass filter, ADC, and MCU, as well as simulation results of key components.

- Chapter 4 discusses the implementation of peripheral modules such as the BME280 sensor, power management, storage, and display.

- Chapter 5 describes the experimental validation of the system, including performance characterization and real hydrogen sensing tests.
- Chapter 6 concludes the thesis and discusses possible directions for future research.

CHAPTER TWO

IONIC-LIQUID HYDROGEN SENSOR AND ELECTRODE CHIP

2.1 Principle of Ionic-Liquid Hydrogen Sensor

Electrochemical hydrogen sensors operate based on the redox processes that generate an electrical signal proportional to the concentration of hydrogen in the surrounding environment [2, 5, 14, 15]. Among them, the IL H_2 sensor sensor employs noble metal catalysts, such as Pt or Pd, as the working electrode in an ionic liquid electrolyte [7, 10, 16]. Hydrogen is electrochemically oxidized directly on the catalytic surface according to:

$$H_2 \rightarrow 2H^+ + 2e^- \tag{2.1}$$

When hydrogen gas reaches the Working Electrode (WE), it dissociates on the Pt/Pd surface and is oxidized, generating protons and electrons. The electrons flow through the external circuit toward the CE, producing a measurable current. The resulting current is proportional to the hydrogen partial pressure, enabling quantitative detection [8, 17].

Compared with traditional aqueous electrolyte systems, ionic liquid electrolytes provide superior chemical stability, low volatility, and wide electrochemical windows [9, 10, 16]. These properties improve sensor durability and allow miniaturization and integration of noble-metal electrodes on a microfabricated chip platform [7, 10].

2.2 Electrode Chip Structure

The IL H_2 sensor sensor relies on a microfabricated electrode chip, which typically consists of:

- **Working Electrode (WE):** A noble metal electrode (e.g., Pt or Pd) where hydrogen molecules are catalytically dissociated and electrochemically oxidized in the ionic liquid environment. The electrode surface properties, catalytic activity, and micro/nano-structuring critically determine the sensitivity and response time of the sensor [7, 8, 18].

- **Reference Electrode (RE):** Provides a stable reference potential against which the WE is biased. Ionic-liquid-compatible quasi-reference electrodes (such as Pt or Ag/AgCl in IL systems) are commonly employed to ensure stable and reproducible operation [9, 10].

- **Counter Electrode (CE):** Completes the electrochemical circuit by providing a surface for the complementary charge-balancing reaction. The CE typically features a large surface area noble metal to ensure stable current flow and long-term durability [7, 10].

Figure 2.1 shows the WE, CE, and RE layout. The electrodes are typically fabricated using Micro-Electro-Mechanical Systems (MEMS) processes, such as photolithography and thin-film deposition [7, 19], which enable precise patterning, reproducibility, and compatibility with portable integration. The chip design also allows batch production and scalability, which are advantageous for commercialization and deployment in IoT-based hydrogen sensing platfoRoot Mean Square (RMS) [5, 8, 20].

2.3 Output Characteristics of The IL H_2 Sensor

The IL H_2 sensor generates ultra-low current outputs due to the limited redox reaction rate in the ionic liquid. Typical characteristics include:

- **Current magnitude:** pA–nA range under standard hydrogen concentrations [7, 10].

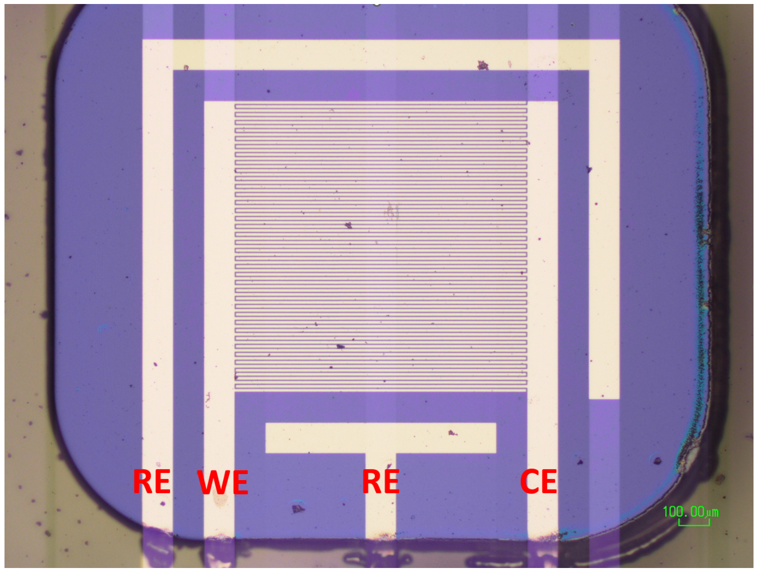

Figure 2.1: Photograph of the electrode chip showing the working electrode (WE), reference electrode (RE), and counter electrode (CE).

- **Linearity:** The output current is approximately proportional to hydrogen partial pressure [8, 16].
- **Bias dependence:** The sensor current strongly depends on the applied potential between WE and RE, highlighting the importance of a stable and programmable potentiostat circuit [11, 12].
- **Environmental sensitivity:** Temperature, humidity, and pressure may influence ionic conductivity and electrode kinetics, requiring compensation in practical systems [7, 17].

Figure 2.2 shows the IL H_2 sensor signal at different hydrogen concentrations.

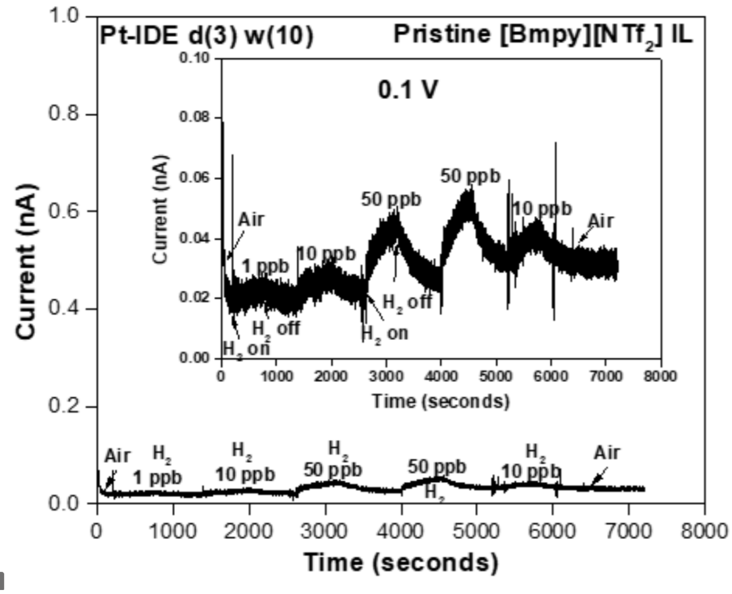

Figure 2.2: Output characteristic of ionic-liquid Hydrogen Sensor.

2.4 Implications For Readout Circuit Design

The characteristics of the IL H_2 sensor and its electrode chip impose strict requirements on the readout electronics:

- A stable potentiostat circuit to control the electrode bias potential [12].
- Ultra-high sensitivity current measurement capability (down to pA level) [11].
- Low noise and leakage minimization in both circuit design and PCB layout [11, 21].
- Integration of environmental monitoring to compensate for external influences [7, 14].

Figure 2.3 shows the overall block diagram of the readout circuit. The IL H_2 sensor and its electrode chip provide a promising platform for hydrogen detection with high sensitivity and miniaturization potential [7]. However, the extremely low output current necessitates a carefully designed readout system, which will be detailed in the subsequent chapters.

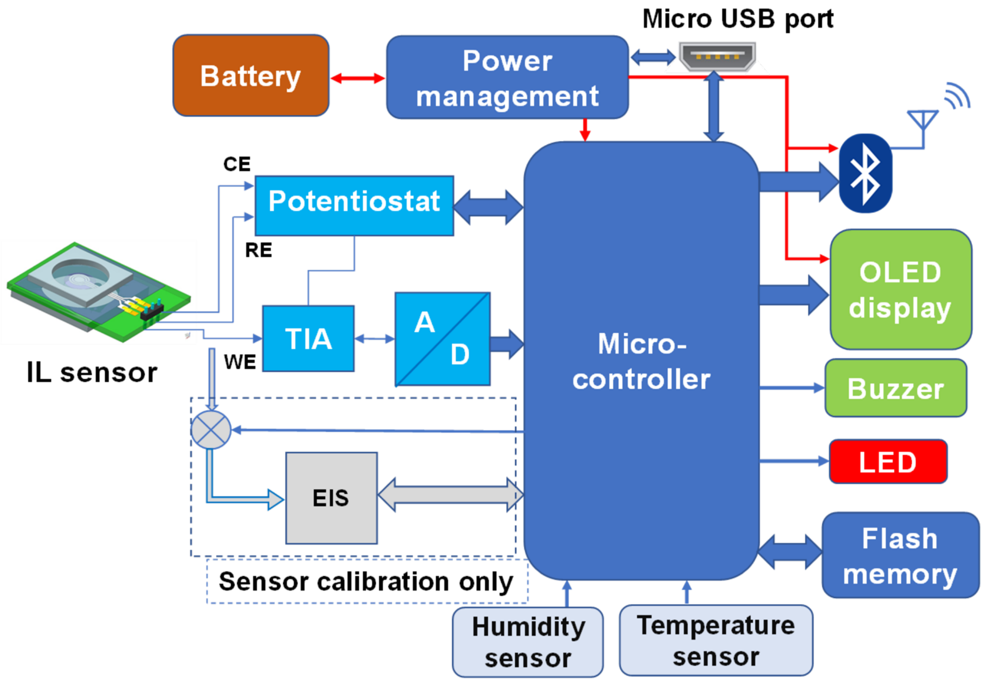

Figure 2.3: Overall block diagram of the hydrogen sensor readout system.

CHAPTER THREE

CORE READOUT CIRCUIT DESIGN

The IL H_2 sensor generates ultra-low current signals in the range of picoamperes to nanoamperes. To acquire such weak signals reliably, a dedicated readout circuit is required. The readout chain must not only amplify and filter the sensor output but also provide a stable electrode bias, digitize the signal with high resolution, and enable real-time control of operating parameters.

In this chapter, the design of the core readout circuit is presented. The system is organized as a complete signal chain starting from the sensor electrodes and ending at the digital domain. Specifically, a potentiostat circuit maintains the electrode bias, with its reference voltage supplied by a DAC under MCU control. The sensor current is then converted into voltage by a TIA, followed by a second-order low-pass filter to suppress noise. The filtered signal is digitized by a high-resolution ADC, and all modules are coordinated by the MCU, which also manages user interaction via push buttons.

The following sections provide a detailed description of each module, including the potentiostat, DAC and MCU interface, TIA, low-pass filter, ADC, and MCU. Design principles, circuit topologies, and implementation considerations are discussed in detail.

3.1 Potentiostat Circuit

The potentiostat is the core circuit used to maintain a constant potential between WE and the RE of the IL H_2 sensor. Since the electrode current is in the pA–nA range, the choice of operational amplifier is critical to ensure low noise, low offset, and high stability [9, 12].

3.1.1 Operational Amplifier Selection and Performance Comparison

Several precision Operational Amplifier (OP Amp) commonly used in electrochemical sensing applications were compared to guide the device selection. Table 3.1 summarizes their key performance parameters.

Table 3.1: Comparison of OPA189 with typical operational amplifiers for potentiostat circuits

OP Amp	Input Bias Current	Offset Voltage	Noise Density	Bandwidth
OPA189 (TI)	5 pA	5 µV	5.7 nV/$\sqrt{\text{Hz}}$	14 MHz
OPA197 (TI)	20 pA	25 µV	8 nV/$\sqrt{\text{Hz}}$	10 MHz
OPA333 (TI)	70 pA	10 µV	55 nV/$\sqrt{\text{Hz}}$	350 kHz
AD8628 (ADI)	1 pA	25 µV	22 nV/$\sqrt{\text{Hz}}$	2.5 MHz
LMP7721 (TI)	3 fA	20 µV	6 nV/$\sqrt{\text{Hz}}$	17 MHz

From the comparison, the OPA189 demonstrates an excellent trade-off between ultra-low offset voltage, low bias current, low noise density, and wide bandwidth. Although the LMP7721 offers femtoampere-level input bias currents, its cost and stability limitations make OPA189 a more reliable choice for this application [22]. Therefore, OPA189 was selected as the core amplifier for the potentiostat circuit.

3.1.2 Circuit Design

Figure 3.1 shows the schematic of the potentiostat. The DAC provides the reference bias voltage (DAC_OUT), which is applied through the feedback network to maintain a stable potential between WE and RE, while the CE balances the current.

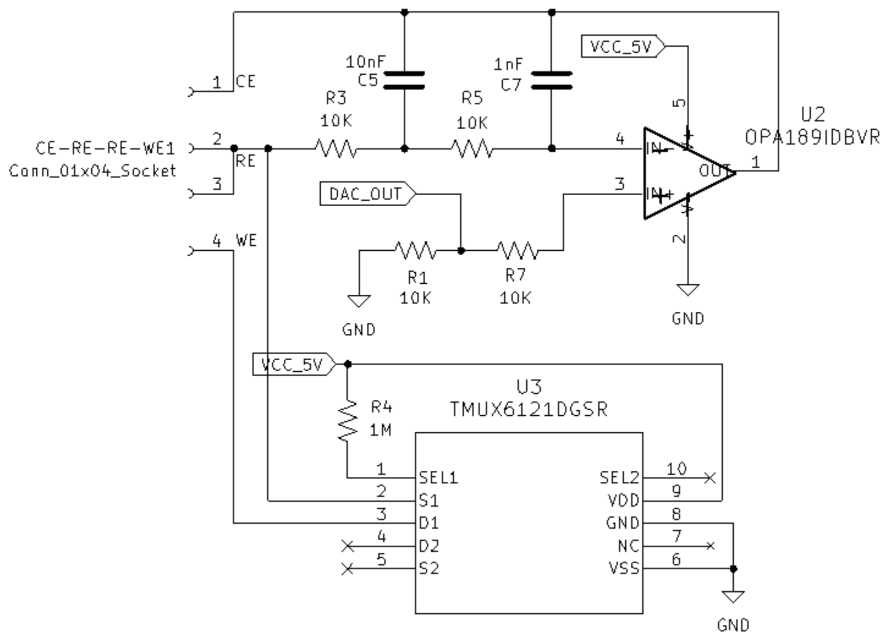

Figure 3.1: Schematic of the potentiostat circuit using OPA189.

- **DAC bias control:** The MCU-controlled DAC allows flexible switching between DC and AC excitation, enabling advanced electrochemical testing.
- **Feedback network:** A resistor–capacitor compensation network consisting of R3 (10 kΩ),R5 (10 kΩ), C5 (10 nF), and C7 (1 nF) improves loop stability and suppresses high-frequency noise in the TIA.
- **Power-off protection:** A TMUX6121 analog switch shorts WE and RE during power-off, preventing residual charges from obstructing the next startup. This block was omitted in simulation since it only affects power-off behavior [23].

3.1.3 Simulation Results

The circuit was simulated using TINA-TI to evaluate DC accuracy, AC response, and noise performance.

- **DC accuracy:** The potential difference V_{WE-RE} follows the DAC input with error less than 1 mV.
- **AC response:** Sinusoidal input waveforms were tracked accurately across 1–100 Hz without distortion.
- **Stability:** Compensation capacitors ($C5 = 10$ nF, $C7 = 1$ nF) effectively suppressed oscillations, ensuring stable closed-loop behavior.
- **Noise:** Simulations confirmed significant reduction of broadband noise, preserving sensor signal integrity.

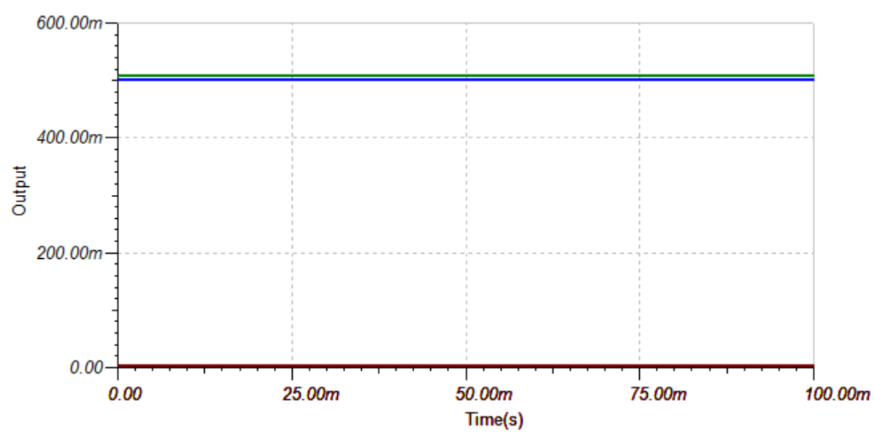

Figure 3.2: TINA simulation results of the potentiostat (DAC: BLUE, RE: GREEN, CE: RED).

As a result, the OPA189-based potentiostat circuit achieves precise and stable electrode bias control with low noise and high accuracy. Both design analysis and simulation results confirm that it provides a robust foundation for ultra-low current hydrogen sensing.

3.2 DAC and MCU Control Interface

The DAC is responsible for generating the programmable bias voltage required by the potentiostat circuit. In this design, the DAC not only provides a DC offset for stable electrode biasing, but also supports the addition of an AC component, allowing the system to perform both steady-state and dynamic electrochemical measurements. This enables advanced tests such as impedance spectroscopy by applying sinusoidal or square-wave perturbations.

3.2.1 DAC Performance Comparison

Table 3.2 compares DAC80502 with several commonly used DACs in sensor readout systems. Key metrics include resolution, interface type, reference source, output range, and typical noise.

Table 3.2: Comparison of DAC80502 with typical DACs for precision biasing applications

DAC	**Resolution**	**Channels**	**Interface**	**Noise (typ.)**
DAC80502 (TI)	16-bit	2	I^2C / SPI	3 µV RMS
MCP4725 (Microchip)	12-bit	1	I^2C	85 µV RMS
AD5696 (ADI)	16-bit	4	I^2C / SPI	7 µV RMS
DAC7571 (TI)	12-bit	1	I^2C	50 µV RMS
LTC2602 (ADI)	16-bit	2	SPI	5 µV RMS

From the comparison, DAC80502 provides a strong balance of high resolution, low noise, dual-channel flexibility, and compatibility with both Serial Peripheral Interface (SPI) and Inter-Integrated Circuit (I^2C) interfaces. Its low noise floor and internal reference make it especially well-suited for precision potentiostat biasing [24].

3.2.2 DAC Circuit Implementation

The chosen device is the Texas Instruments DAC80502, a dual-channel, 16-bit precision DAC with low noise and excellent linearity. Channel A (VOUTA) is used to generate the potentiostat bias voltage (DAC_OUT). The DAC is powered from a 3.3 V supply, with decoupling capacitors (1 μF and 0.1 μF) placed near VDD to ensure supply stability.

As shown in Figure 3.3, the SPI2C pin of DAC80502 is pulled high through a 10 kΩ resistor, configuring the device to operate in I^2C mode. In this mode, the DAC shares the I^2C bus with other peripherals such as the BME280 (environmental sensor) and SSD1306 (OLED display), reducing the number of required MCU pins.

3.2.3 MCU Communication and User Interface

The DAC80502 communicates with the MCU via the shared I^2C bus. The MCU firmware allows users to adjust DAC outputs through three push buttons:

- **Mode button:** Switches between control modes: AC frequency, AC amplitude, and DC offset.
- **Increment button:** Increases the selected parameter.
- **Decrement button:** Decreases the selected parameter.

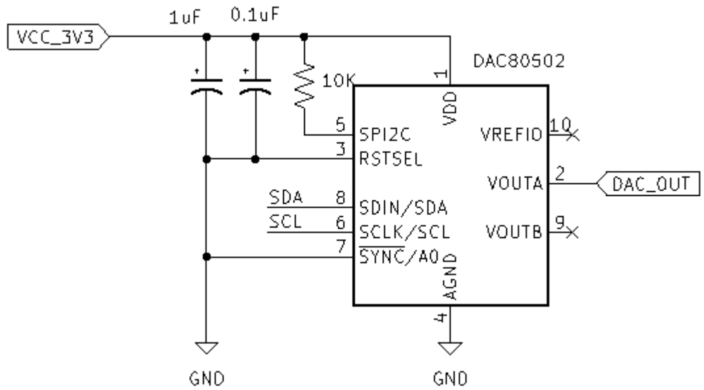

Figure 3.3: Schematic of the DAC80502 circuit. The SPI2C pin is pulled up with 10 kΩ to enable I^2C mode.

This design allows the DAC output to be flexibly adjusted in real time, supporting both static biasing and dynamic excitation.

3.3 Transimpedance Amplifier (TIA)

The IL H_2 sensor generates extremely small currents in the picoampere to nanoampere range. Direct voltage measurement is impractical due to the high electrode impedance and susceptibility to noise [11]. Instead, a TIA is used to convert the input current (I_{in}) into a measurable voltage (V_{out}):

$$V_{out} = -I_{in} \times R_f \tag{3.1}$$

where R_f is the feedback resistor. This configuration provides both high sensitivity and low output impedance, enabling subsequent filtering and digitization.

3.3.1 Comparison with General-purpose OP Amp Based Current-to-Voltage Conversion

A current-to-voltage converter can be constructed using a general-purpose operational amplifier with a feedback resistor, forming a basic transimpedance stage. However, there are important differences between such implementations and dedicated TIAs like OPA380.

- **Input bias current:** General-purpose OP Amp often have input bias currents in the tens of picoamperes or higher, which introduces significant error when measuring sensor currents in the pA–nA range. Dedicated TIAs such as OPA380 or LMP7721 feature ultra-low bias currents (fA–pA), minimizing measurement error.

- **Noise performance:** The input voltage and current noise of general-purpose OP Amp are typically higher, leading to poor Signal-to-Noise Ratio (SNR) for ultra-low current signals. Specialized TIA amplifiers are optimized for low-noise transimpedance applications, ensuring better detection of weak sensor currents.

- **Stability with large feedback resistors:** Using very high-value feedback resistors (in the MΩ–GΩ range) with general OP Amp often causes instability and oscillation due to limited Gain Bandwidth Product (GBW). TIAs like OPA380 are designed with high GBW (90 MHz), allowing stable operation even with large feedback resistors.

- **Parasitics and compensation:** In general OP Amp circuits, parasitic capacitance across high-value resistors can cause peaking or instability. Compensation capacitors must be carefully tuned manually. Dedicated TIA amplifiers integrate optimized compensation, simplifying design and improving robustness.

- **Dynamic range and linearity:** While general OP Amp can achieve current-to-voltage conversion, their linearity and dynamic range are often insufficient for ultra-low current measurements. TIA-specific devices are optimized to maintain linear response from fA up to µA currents.

Although a general-purpose OP Amp with a feedback resistor can technically perform current-to-voltage conversion, its limitations in bias current, noise, stability, and bandwidth make it unsuitable for ultra-low current sensing. By contrast, dedicated TIAs such as OPA380 provide higher sensitivity, lower noise, and more robust operation, which are essential for the hydrogen sensor readout system.

3.3.2 Performance Comparison of TIA

The choice of operational amplifier is critical for TIA design, as input bias current, input noise, and gain bandwidth directly affect sensitivity and accuracy. Table 3.3 compares several commonly used TIAs or OP Amp suitable for transimpedance applications.

Table 3.3: Comparison of operational amplifiers for TIA applications

OP Amp	**Input Bias Current**	**Noise Density**	**GBW**
OPA380 (TI)	0.2 pA	$5\ nV/\sqrt{Hz}$	90 MHz
OPA140 (TI)	10 pA	$5.1\ nV/\sqrt{Hz}$	11 MHz
OPA129 (TI)	100 fA	$15\ nV/\sqrt{Hz}$	500 kHz
LMP7721 (TI)	3 fA	$6\ nV/\sqrt{Hz}$	17 MHz
AD8606 (ADI)	1 pA	$12\ nV/\sqrt{Hz}$	10 MHz

From the comparison, the OPA380 was chosen for this design due to its combination of very low input bias current, wide bandwidth, and excellent noise performance, making it highly suitable for low-current hydrogen sensing [25, 26].

3.3.3 Circuit Implementation and Analysis

Figure 3.4 shows the schematic of the implemented TIA based on OPA380. The circuit is designed to handle input currents down to the picoampere range with high fidelity.

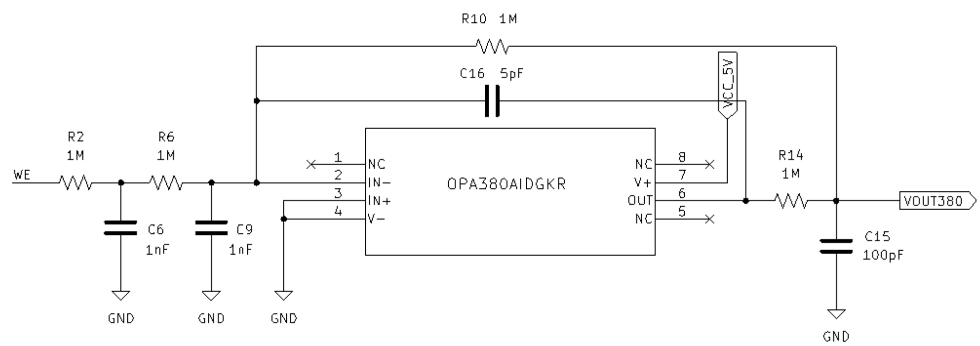

Figure 3.4: Schematic of the transimpedance amplifier (TIA) based on OPA380.

Key features of the circuit include:

- **Feedback network:** R10 (1 MΩ) converts input current into output voltage, while C16 (5 pF) stabilizes the amplifier and sets the bandwidth.
- **Input protection:** R2 and R6 (1 MΩ each) in series with C6 and C9 (1 nF each) filter out high-frequency interference and limit input surge currents.

- **Output filter:** R14 (1 MΩ) and C15 (100 pF) form a simple RC filter at the output to further suppress high-frequency noise before digitization.
- **TIA choice:** The OPA380 provides ultra-low input bias current (0.2 pA) and high GBW (90 MHz), ensuring low noise and fast settling.

3.3.4 Simulation Results

The TIA was simulated using TINA software to evaluate linearity, stability, and noise performance.

- **Linearity:** The output voltage showed a linear relationship with input current in the range of 10 pA to 1 μA, with negligible distortion.
- **Stability:** The 5 pF feedback capacitor ensured stable closed-loop behavior, preventing oscillations even at high gain.
- **Noise performance:** The simulated noise floor was below 5 pA RMS, confirming suitability for picoampere-level current detection.
- **Bandwidth:** The effective bandwidth was approximately 100 kHz, sufficient for hydrogen sensor signals (0–100 Hz).

3.3.5 Experimental Validation of OPA380 TIA

In addition to simulations, the OPA380-based TIA circuit was fabricated and experimentally tested to evaluate its real-world performance with ultra-low input currents. The measurement setup included a precision current source to emulate the hydrogen sensor output and a high-resolution oscilloscope/data acquisition system to record the TIA output.

The test results confirmed the expected performance:

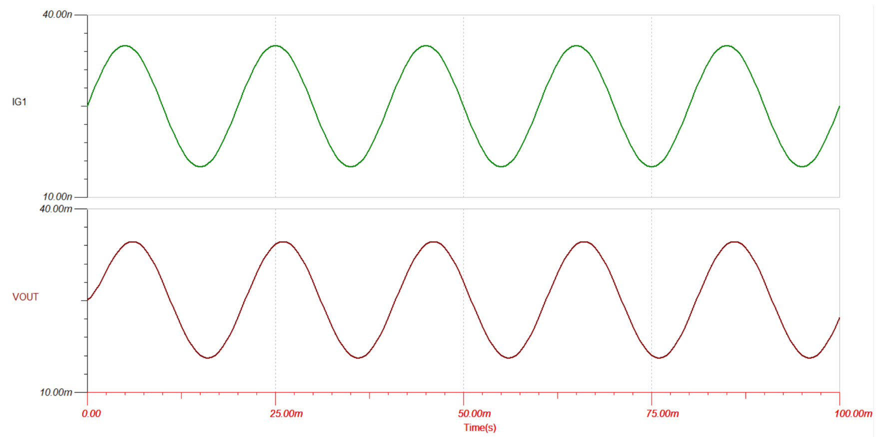

Figure 3.5: Simulation results of the TIA: input current vs. output voltage.

- **Linearity:** The measured output voltage exhibited a clear linear relationship with the input current over the range of 10 pA to 1 µA, consistent with the designed transimpedance gain.

- **Noise:** The measured noise floor was consistent with the simulation results, remaining below 5 pA RMS. This validates the suitability of the OPA380 for picoampere-level sensing applications.

- **Stability:** No oscillations or instability were observed, confirming that the feedback capacitor (5 pF) provided sufficient loop compensation.

- **Dynamic response:** The TIA showed fast settling when subjected to step current inputs, demonstrating that the 90 MHz GBW of OPA380 provides adequate headroom for this application.

Figure 3.7 shows the experimental measurement results of the OPA380 TIA, illustrating both the linear current-to-voltage response and the low-noise characteristics.

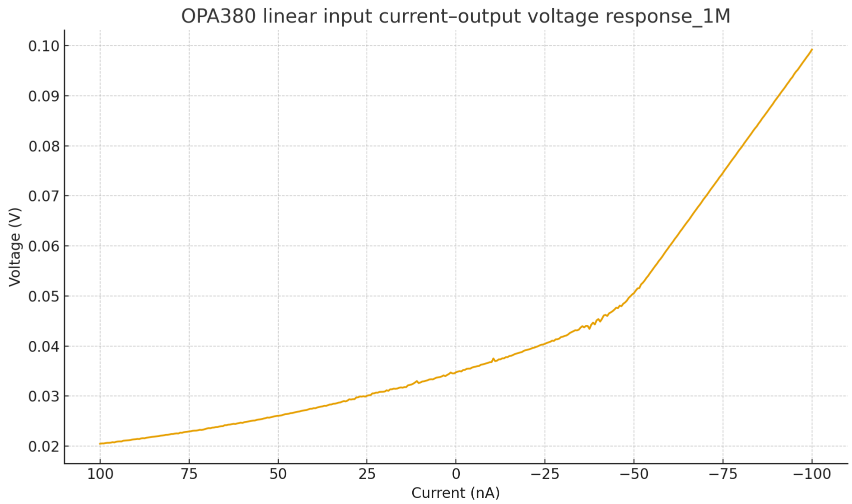

Figure 3.6: OPA380 linear sweep I-V response.

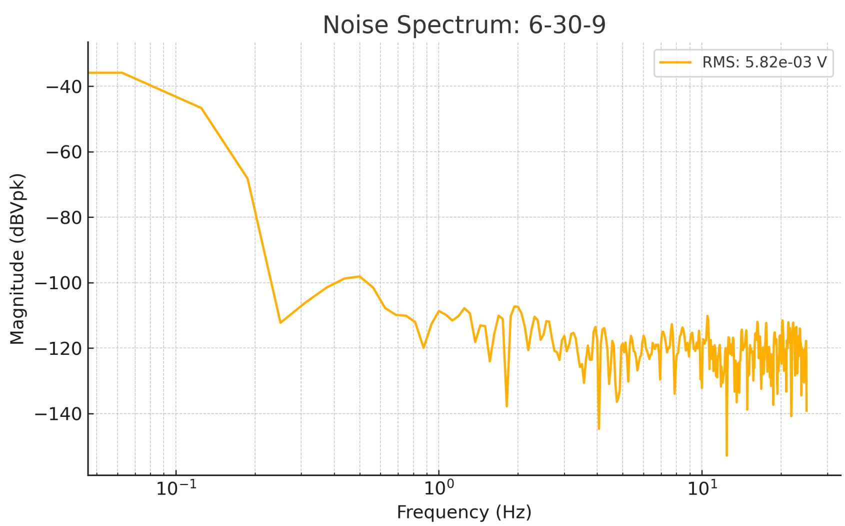

Figure 3.7: TIA output voltage spectral noise density. RMS noise voltage value is also included.

The experimental validation thus confirms that the OPA380-based TIA not only meets the theoretical and simulated performance targets but also delivers stable, accurate, and low-noise current-to-voltage conversion in practice.

3.4 Second-order Low-pass Filter

3.4.1 Purpose of the Filter

The ultra-low current signal from the TIA still contains high-frequency noise components arising from environmental interference, DAC switching artifacts, and intrinsic circuit noise. Since the hydrogen sensing signal of interest lies in the low-frequency band (typically below 100 Hz), a second-order low-pass filter is implemented to attenuate high-frequency noise while preserving the relevant sensing information [27].

3.4.2 Circuit Implementation

Figure 3.8 shows the schematic of the implemented second-order low-pass filter. The circuit adopts a multiple-feedback (MFB) topology, which provides accurate cutoff frequency control and high roll-off rate.

The circuit is designed using the OPA189 precision OP Amp for its low noise and high stability. Key components include:

- **Input resistor:** R12 (10 kΩ), which limits input surge currents and provides basic input protection.
- **Feedback resistors:** R13 (10 kΩ) and R11 (10 kΩ), forming the feedback path to set transimpedance gain and improve loop stability.
- **Capacitors:** C23 (750 pF) and C18 (3.3 nF), acting as frequency compensation and noise filtering components to suppress high-frequency interference.

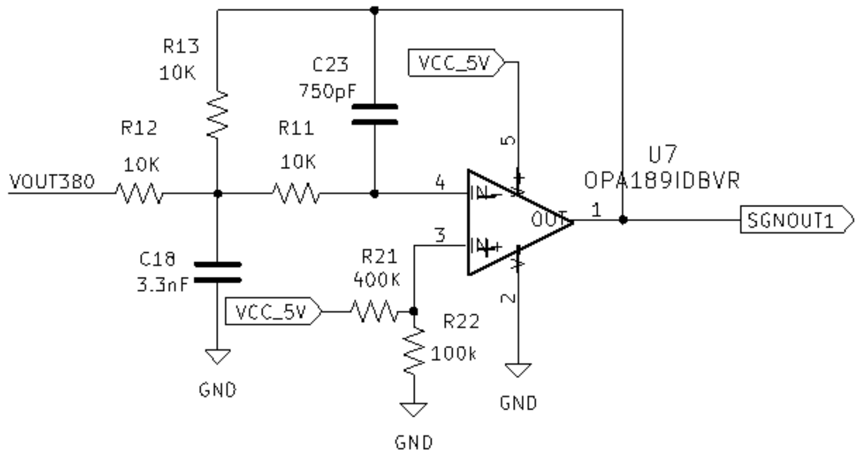

Figure 3.8: Schematic of the second-order low-pass filter based on OPA189.

- **Voltage divider bias:** R21 (400 kΩ) and R22 (100 kΩ), establishing a stable DC bias voltage for the OP Amp to ensure proper operating point.

The theoretical cutoff frequency f_c of the filter can be approximated by:

$$f_c = \frac{1}{2\pi\sqrt{R_1 R_2 C_1 C_2}} \tag{3.2}$$

With the chosen values, the cutoff frequency is 9kHz, which matches the bandwidth requirements of the hydrogen sensing signal.

3.4.3 Simulation Results

The circuit was simulated in TINA to verify its frequency response and noise suppression capability.

- **Frequency response:** The Bode plot a cutoff frequency around 16 Hz, with a -40 dB/decade roll-off beyond the cutoff.

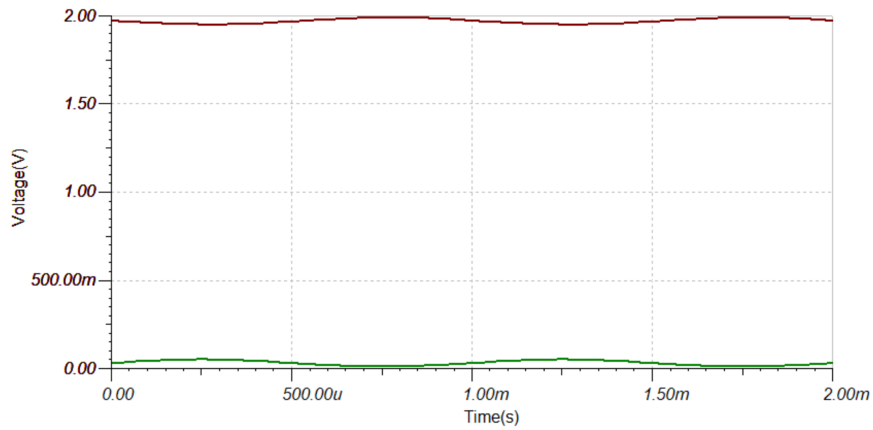

Figure 3.9: Simulation results of the second-order low-pass filter: 1k frequency response and phase characteristics.

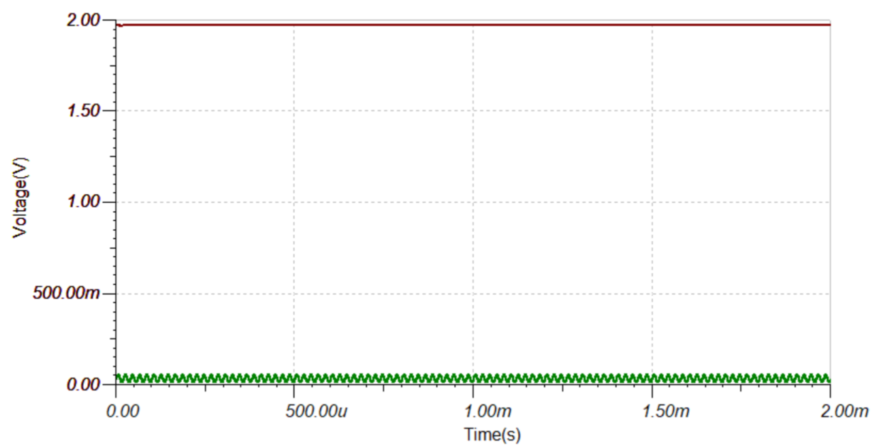

Figure 3.10: Simulation results of the second-order low-pass filter: 50k frequency response and phase characteristics.

- **Phase response:** The filter maintains stable phase characteristics in the passband, avoiding distortion of low-frequency signals.

- **Noise suppression:** High-frequency noise above 100 Hz is strongly attenuated, ensuring that only the relevant sensing signal passes to the ADC.

3.5 ADC and MCU Architectures

To digitize the ultra-low current signals from the sensor front-end, two system architectures were evaluated:

1. **Method 1:** High-resolution external ADC (ADS1262) combined with a low-power Bluetooth MCU (CC2640R2F) [28, 29].

2. **Method 2:** MCU MSP430F6736AIPNR with integrated 24-bit sigma-delta ADC [30].

Both approaches have unique advantages, and their characteristics are compared in the following subsections.

3.5.1 Method 1: ADS1262 + CC2640R2F

In this approach, the ADS1262 external ADC provides state-of-the-art resolution and noise performance, while the CC2640R2F MCU handles data acquisition, processing, and Bluetooth communication.

3.5.1.1 Independent ADC Performance Comparison

Table 3.4 compares ADS1262 with several commonly used high-resolution ADCs in precision sensing applications.

The ADS1262 offers an excellent balance of high resolution, low noise, and moderate sampling speed, making it highly suitable for the hydrogen sensor readout system.

Table 3.4: Comparison of high-resolution ADCs for precision sensor readout

ADC	Resolution	Noise (typ.)	Max Sample Rate	Interface
ADS1262 (TI)	24-bit	7 nV/$\sqrt{\text{Hz}}$	38.4 kSPS	SPI
ADS1256 (TI)	24-bit	17 nV/$\sqrt{\text{Hz}}$	30 kSPS	SPI
LTC2400 (ADI)	24-bit	200 nV RMS	6.9 SPS	SPI
AD7768 (ADI)	24-bit	10 nV/$\sqrt{\text{Hz}}$	256 kSPS	SPI
MAX11270 (Maxim)	24-bit	15 nV/$\sqrt{\text{Hz}}$	64 kSPS	SPI

3.5.1.2 MCU Selection: CC2640R2F The CC2640R2F was chosen for its integration of a low-power ARM Cortex-M3 core and Bluetooth Low Energy (BLE) stack. Compared with typical MCUs, CC2640R2F offers:

- **Ultra-low power:** Active mode current $<$ 10 mA, standby current $<$ 1 μA.
- **Wireless connectivity:** BLE 5.0 support enables real-time data transmission.
- **Compact design:** Reduces the need for an external wireless module.
- **Comparison:** Relative to STM32 Cortex-M0/M3 series, CC2640R2F provides lower power consumption and native BLE stack integration.

This combination (ADS1262 + CC2640R2F) is well-suited for portable sensing platforms requiring high accuracy and wireless communication.

3.5.2 Method 2: MSP430F6736AIPNR with On-chip ADC

The second approach uses the Texas Instruments MSP430F6736AIPNR MCU, which integrates a 24-bit sigma-delta ADC. This solution eliminates the need for a separate ADC and reduces system complexity.

3.5.2.1 Advantages of Integrated ADC

- **Compact design:** Combining ADC and MCU in a single chip reduces PCB area and BOM cost.
- **Low noise:** The integrated ADC benefits from short signal paths, reducing susceptibility to interference.
- **Power efficiency:** MSP430 family is optimized for ultra-low-power operation, making it suitable for long-term battery-powered sensing.
- **Simplified communication:** No need for SPI bus interfacing between MCU and ADC, reducing software complexity.

3.5.2.2 Comparison with Method 1 Compared with the external ADC + MCU solution, the MSP430 integrated solution offers lower system cost, smaller size, and potentially lower noise due to reduced wiring. However, it lacks wireless communication capability and may provide slightly lower performance than the dedicated ADS1262 in terms of noise floor and dynamic range.

3.5.3 Summary

Two architectures were explored for ADC and MCU implementation:

- **Method 1 (ADS1262 + CC2640R2F):** Best suited for high-performance, wireless-enabled sensing.
- **Method 2 (MSP430F6736AIPNR):** Offers a compact, low-cost, low-noise integrated solution ideal for battery-powered or resource-constrained systems.

The choice between the two approaches depends on the target application: whether maximum performance and wireless connectivity are required, or whether simplicity and low power consumption are prioritized.

CHAPTER FOUR

PERIPHERAL FUNCTIONAL MODULES

In addition to the core readout circuit, several peripheral modules are required to ensure the robustness, portability, and usability of the hydrogen sensor system. These modules provide environmental compensation, stable power supply, data logging, and user interaction, thereby enabling the transition from a laboratory prototype to a practical portable sensing platform. This chapter introduces the design and implementation of these functional modules.

4.1 Environmental Monitoring (BME280)

4.1.1 Sensor Performance Comparison

To ensure reliable hydrogen sensing, it is important to monitor the ambient environment. Table 4.1 compares BME280 with several commonly used temperature, humidity, and pressure sensors.

Table 4.1: Comparison of environmental sensors for portable applications

Sensor	**Temperature Accuracy**	**Humidity Accuracy**	**Pressure Accuracy**
BME280 (Bosch)	±0.5°C	±3% RH	±1 hPa
BMP280 (Bosch)	±1.0°C	–	±1 hPa
SHT31 (Sensirion)	±0.3°C	±2% RH	
HTU21D (TE)	±0.3°C	±2% RH	–

From the comparison, BME280 provides a balanced and compact solution by integrating all three parameters (temperature, humidity, pressure) into a single package, reducing component count and simplifying calibration [31–34].

4.1.2 Data Calculation from BME280

The BME280 outputs raw ADC values for temperature, humidity, and pressure. These raw readings must be converted into physical units using factory calibration coefficients.

For example, the temperature calculation is based on a polynomial correction:

$$T = \frac{T_{raw}}{16384.0} - \frac{digT1}{1024.0} \tag{4.1}$$

$$T_{comp} = T \cdot digT2 + \left(\frac{T}{8.0}\right)^2 \cdot digT3 \tag{4.2}$$

where T_{raw} is the raw ADC output, and $digT1$, $digT2$, $digT3$ are calibration coefficients stored in the sensor.

Similarly, pressure and humidity values are obtained using multi-variable polynomial correction with their respective calibration constants. The corrected results are then expressed in SI units: temperature (°C), pressure (Pa), humidity (RH%) [35].

4.1.3 Environmental Data Fitting with Electrochemical Signal

The measured electrochemical current from the hydrogen sensor is influenced by environmental conditions. For instance, the ionic liquid conductivity is temperature-dependent, and humidity can affect electrode kinetics. To improve measurement accuracy, a multi-variable regression model is applied:

$$I_{comp} = I_{meas} - \left(a \cdot (T - T_{ref}) + b \cdot (H - H_{ref}) + c \cdot (P - P_{ref})\right) \tag{4.3}$$

where I_{meas} is the raw measured current, I_{comp} is the compensated current, T, H, and P are the temperature, humidity, and pressure obtained from the BME280, and a, b, c are regression coefficients determined experimentally.

4.2 Power Management and Regulation

Stable and low-noise power supply is essential for the hydrogen sensor readout system, since the measured currents are in the picoampere to nanoampere range and even small fluctuations in supply voltage can degrade accuracy. The power management architecture is designed to support both digital and analog circuits with independent regulation, ensuring low-noise analog operation while maintaining efficient battery-powered portability.

4.2.1 Battery and Power Management IC

The system is powered by a **3.7 V, 2000 mAh lithium-ion battery**, which provides sufficient capacity for long-term portable operation. Battery charging and management are handled by the **BQ24074** power management IC [36].

Key features of BQ24074 include:

- **USB Type-C charging interface:** Supports charging through a modern Type-C connector.
- **Battery protection:** Integrated power-path management prevents overcharge, over-discharge, and overheating.

- **Seamless switching:** Automatically manages power between USB input and battery to ensure uninterrupted operation.

4.2.2 Boost Converter

Since many analog components in the readout system require a stable 5 V supply, a step-up converter is employed. The **TPS61022** boost converter raises the 3.7 V battery voltage to 5 V, providing sufficient headroom for the analog circuits, especially the potentiostat and TIA stages [37].

The TPS61022 offers:

- High efficiency even at low input voltages.
- Peak output current capability up to 2 A, sufficient for system load.
- Small external inductor and capacitor requirements, reducing PCB area.

4.2.3 Low-Dropout Regulator

Although the boost converter provides a regulated 5 V supply, additional filtering is necessary to ensure ultra-low noise for sensitive analog circuits [38, 39]. Two instances of **TPS7A4700** LDOs are used to provide separate clean supplies:

- **3.3 V LDO output:** Powers the digital circuits including MCU, DAC, and environmental sensors (BME280, OLED).
- **5 V LDO output:** Powers the analog front-end circuits including potentiostat, TIA, and low-pass filter.

The TPS7A4700 is selected due to its excellent noise performance (4.17 µVrms from 10 Hz to 100 kHz) and high Power Supply Rejection Ratio (PSRR), which are critical for minimizing noise coupling into the analog measurement path.

4.2.4 Simulation of Power Boost Converter and LDO Circuits

To verify the functionality of the designed power chain, simulations were performed for both the boost converter (TPS61022) and the LDO (TPS7A4700). The objective was to confirm that TPS61022 can boost the 3.7 V battery voltage to 5 V, and that TPS7A4700 can provide stable regulation at 3.3 V and 5.0 V for digital and analog domains.

The simulations were carried out using two platforms: TPS61022 was evaluated in Texas Instruments Power Designer, while TPS7A4700 was analyzed in TINA-TI. Figure 4.1 and Figure 4.2 show the simulation schematics, and Figure 4.3 and Figure 4.4 present representative output results.

It is worth noting that, throughout the entire system design, standard resistor, capacitor, and inductor models are sufficient, with one exception: the inductor used in the TPS61022 boost converter requires a low DCR type (recommended DCR < 20 mΩ). Otherwise, the boost system may fail to start and could potentially damage the TPS61022 chip. In this design, a Würth Elektronik 74404043010A inductor (1 μH, 4.9 A, 14 mΩ) was selected to ensure reliable boost converter operation.

The results confirm that the TPS61022 successfully performs boost conversion from 3.7 V to 5 V, while TPS7A4700 achieves low-noise regulation at both 3.3 V and 5.0 V. This validates the proposed architecture for providing reliable and stable power to the hydrogen sensor system.

4.2.5 System Architecture

The complete power architecture is illustrated in Figure 4.5, showing the flow from the lithium-ion battery through charging, boosting, and regulation stages.

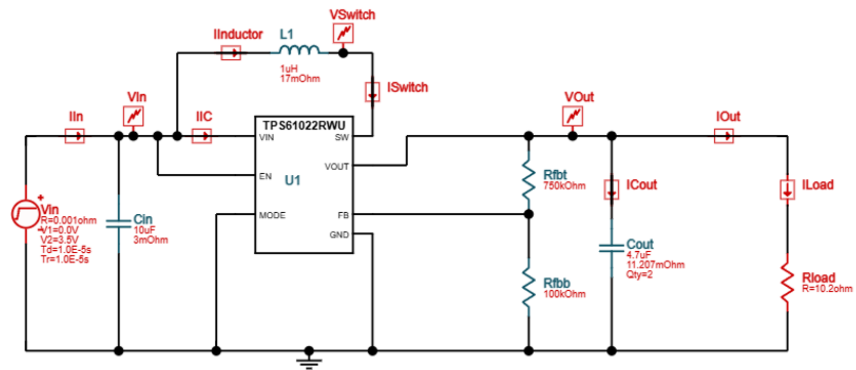

Figure 4.1: TPS61022 boost converter schematic simulated in TI Power Designer.

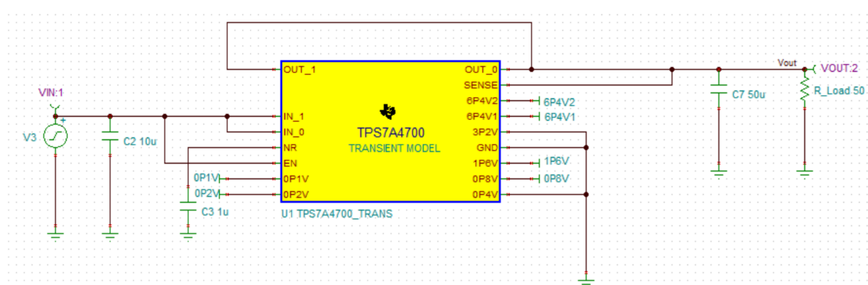

Figure 4.2: TPS7A4700 LDO schematic simulated in TINA-TI.

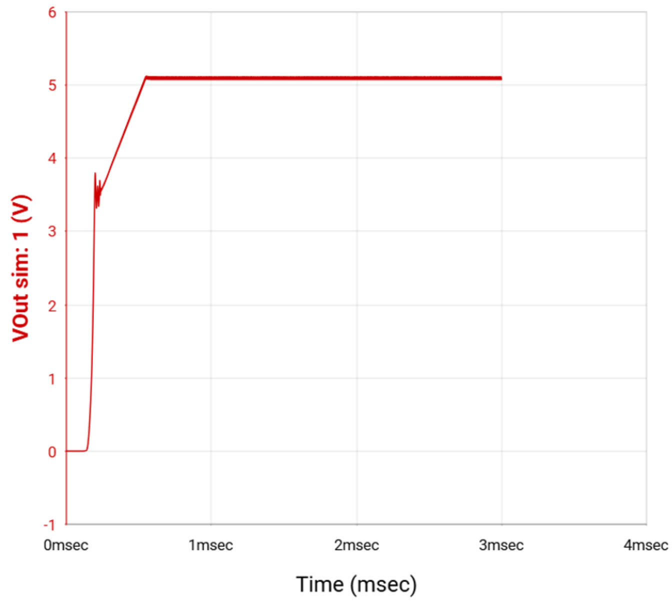

Figure 4.3: Simulation result of TPS61022 showing successful step-up to 5 V from 3.7 V input.

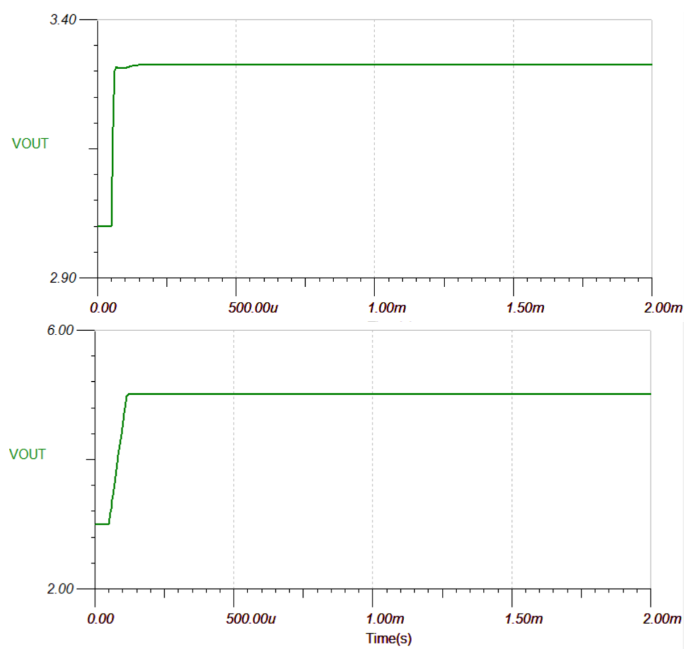

Figure 4.4: Simulation result of TPS7A4700 showing stable regulated outputs at 3.3 V(upper) and 5.0 V(lower).

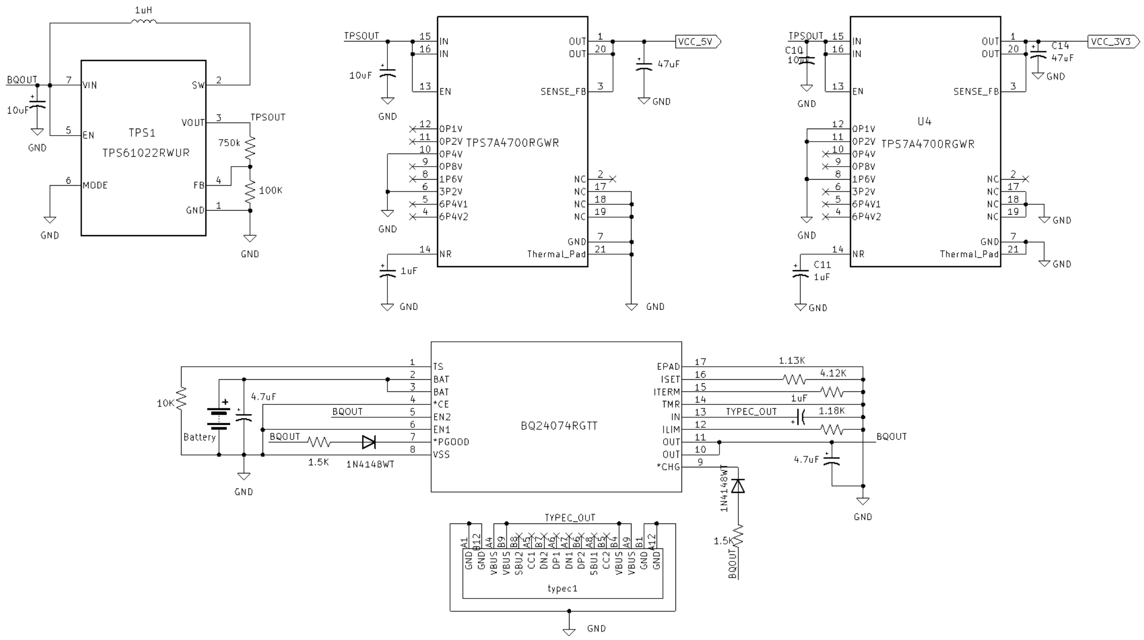

Figure 4.5: Power management and regulation architecture for the hydrogen sensor system.

The power management system integrates a rechargeable lithium-ion battery, charging management via BQ24074, a high-efficiency boost converter (TPS61022), and two ultra-low-noise LDOs (TPS7A4700). This architecture ensures stable and isolated power supplies for digital and analog domains, significantly reducing noise interference and improving the reliability of the sensing system.

4.3 Storage and Display

To support both long-term data logging and real-time visualization, the system integrates a micro Secure Digital (memory card) (SD) card for storage and an OLED module for display.

4.3.1 Data Storage

Data generated by the hydrogen sensor readout system must be recorded for further offline analysis. A **micro SD card** is employed as the storage medium, interfaced with the MCU through the SPI bus. This configuration allows reliable and high-speed data transfer while keeping hardware complexity low. The file system is managed by the MCU firmware, enabling time-stamped recording of measurement data in standard formats (e.g., CSV), which can be easily accessed for post-processing on a PC [40].

Figure 4.6 shows a typical micro SD card, including pins for SPI communication (CS, CLK, MOSI, MISO) and power/ground.

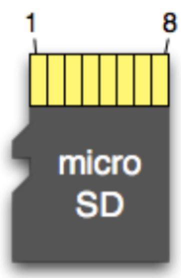

Pin	SD	SPI
1	DAT2	X
2	CD/DAT3	CS
3	CMD	DI
4	VDD	VDD
5	CLK	SCLK
6	VSS	VSS
7	DAT0	DO
8	DAT1	X

Figure 4.6: Pinout of a typical micro SD card socket for SPI mode operation.

4.3.2 Display and User Interface

For real-time feedback, the system includes an SSD1306 OLED display module. The display operates through the I^2C bus, which it shares with the BME280 environmental sensor. The OLED provides a compact 128×64 pixel graphical interface capable of displaying key parameters, including electrode bias settings, measured current, environmental data, and system status [41].

The pinout of the SSD1306 module is shown in Figure 4.7, with the main I^2C pins (SCL, SDA), power supply pins (VCC, GND), and optional control pins (RES, DC, CS).

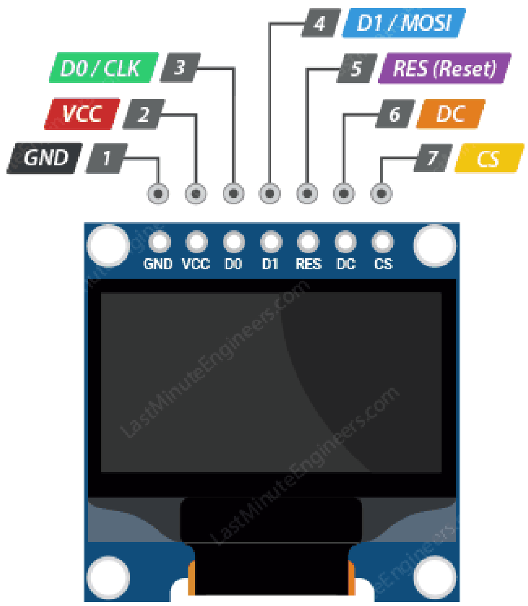

Figure 4.7: Pinout of SSD1306 OLED display module.

In addition to displaying sensor data, the OLED interface is also used to provide menu navigation controlled by the three push buttons described earlier (mode switch, increment, decrement). This combination allows the user to adjust DAC output parameters (AC/DC amplitude and frequency) and view updated system status in real time.

CHAPTER FIVE

EXPERIMENTAL VALIDATION

This chapter presents the experimental validation of the proposed hydrogen sensor readout system. A prototype was fabricated based on the design described in Chapters 3 and 4, and its performance was evaluated using standard instrumentation. The goal of this chapter is to verify that the system achieves the required sensitivity, stability, and portability for practical hydrogen sensing applications.

5.1 System Implementation

Although the simulation of each functional block was already presented in previous chapters, the complete system design and PCB implementation are summarized here.

Figure 5.1 shows the overall system schematic, illustrating the integration of the potentiostat, TIA , second-order low-pass filter, ADC/MCU, and peripheral modules (power management, storage, and display).

The complete schematic was implemented as a multi-layer PCB. Careful attention was paid to separating analog and digital domains, minimizing ground loops, and providing low-noise supply routing for the sensitive TIA and ADC sections. Figure 5.2 shows the PCB layout of the system.

A photograph of the fabricated PCB is shown in Figure 5.3, highlighting the compact integration of the analog front-end, power management, and MCU subsystems.

5.2 Experimental Setup

The experimental platform consists of:

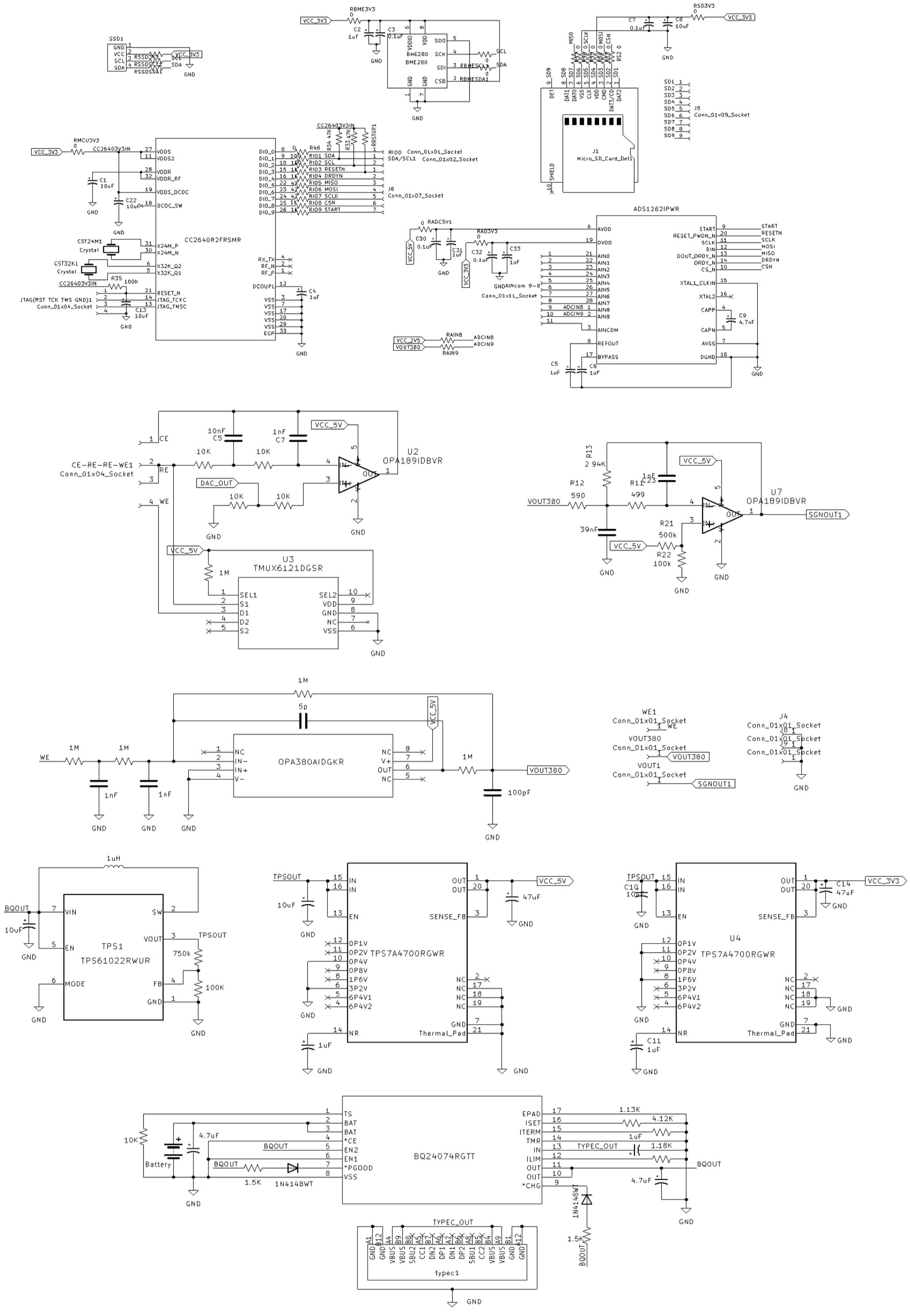

Figure 5.1: Overall system block diagram integrating analog front-end, ADC/MCU, and peripherals.

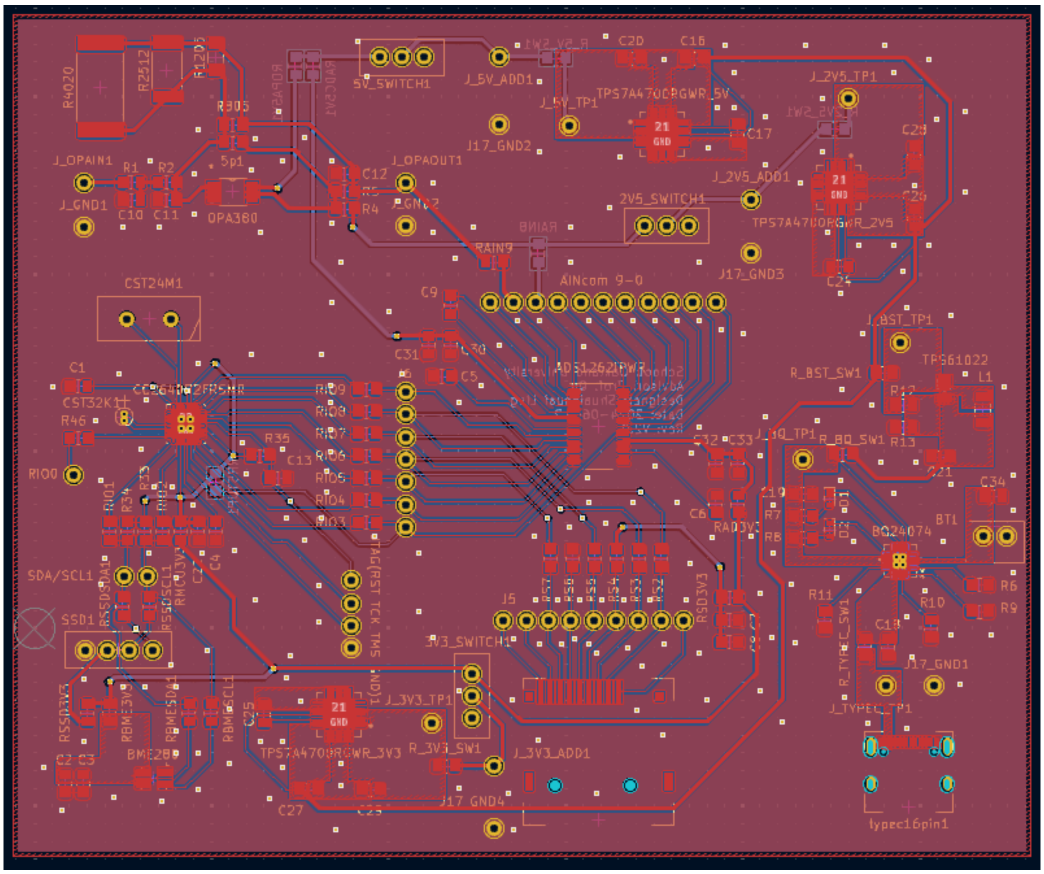

Figure 5.2: PCB layout of the hydrogen sensor readout system.

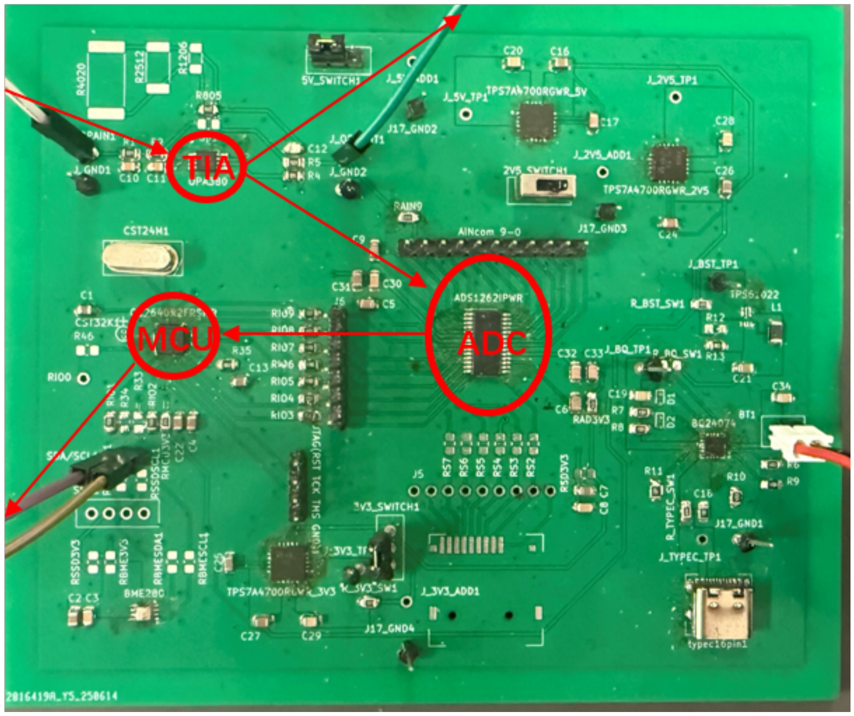

Figure 5.3: Fabricated PCB of the hydrogen sensor readout system.

- The fabricated readout PCB integrating the potentiostat, TIA, low-pass filter, ADC, MCU, and peripheral modules.
- An IL H_2 sensor electrode chip connected to the readout board.
- A Keithley SourceMeter used for reference current measurements and calibration.
- Auxiliary devices for logging, display, and data storage.

The prototype is powered by a rechargeable battery with power management circuits as described in Chapter 4. During experiments, both real-time OLED display and offline SD card logging were used to capture results.

5.3 System Evaluation without Potentiostat

To initially verify the linearity of the readout chain, a calibrated current source was used to perform an I–V scan from 10 pA to 4 nA. The output of the OPA380-based TIA and the digitized values from the ADS1262 ADC were compared against reference Keithley SourceMeter measurements. Figure 5.4 shows the result of this scan, demonstrating excellent linearity across the full input range and confirming the effective transimpedance gain of the gigaohm feedback resistor.

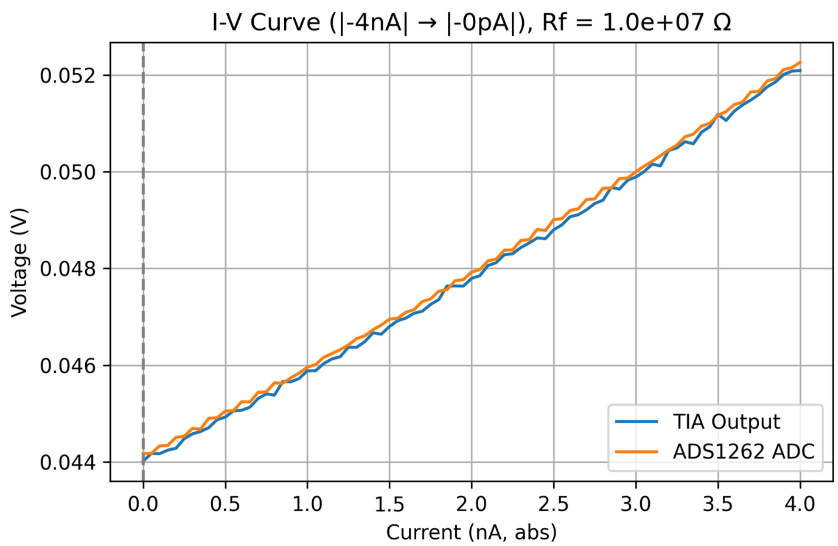

Fig. 4. TIA and ADC output characterization results
I–V curve comparison from 10 pA to 4 nA.

Figure 5.4: I–V linearity scan of the TIA and ADC from 10 pA to 4 nA, showing strong agreement with reference Keithley SourceMeter measurements.

After confirming the intrinsic linearity, the potentiostat was bypassed, and the input current signal was provided by a Keithley 2470 SourceMeter. Rather than being an artificial test signal, the current waveform was based on real hydrogen concentration variation data collected by Prof. Xiangqun Zeng's group at the University of Missouri using a calibrated IL H_2 sensor. This allowed the system to be validated under realistic conditions even without access to a hydrogen chamber in our laboratory.

The current signal was fed directly into the TIA, processed by the low-pass filter, and digitized by the ADC. The resulting data flow through the MCU demonstrated the full functionality of the readout chain.

Figure 5.5 shows a representative comparison of the reference input signal (from the Keithley 2470), the OPA380 TIA output, and the digitized ADC output. The results confirm linear response, consistent transimpedance gain, and correct data acquisition.

5.4 Electrode Chip Integration and Noise Measurement

In the second part of the experiment, the electrode chip was integrated into the readout circuit. A droplet of ionic liquid was applied onto the electrode surface, and the chip was powered on and off to examine startup and shutdown behavior.

Figure 5.6 shows the time-domain results of the IL H_2 sensor during power-up and power-down, demonstrating stable startup characteristics and no residual current after shutdown.

To further characterize the sensor baseline, the time-domain noise was measured with the IL H_2 sensor connected but not powered on. As shown in Fig. 5.7, the measured signal remained within the expected noise floor range, confirming the absence of spurious leakage currents in the idle state.

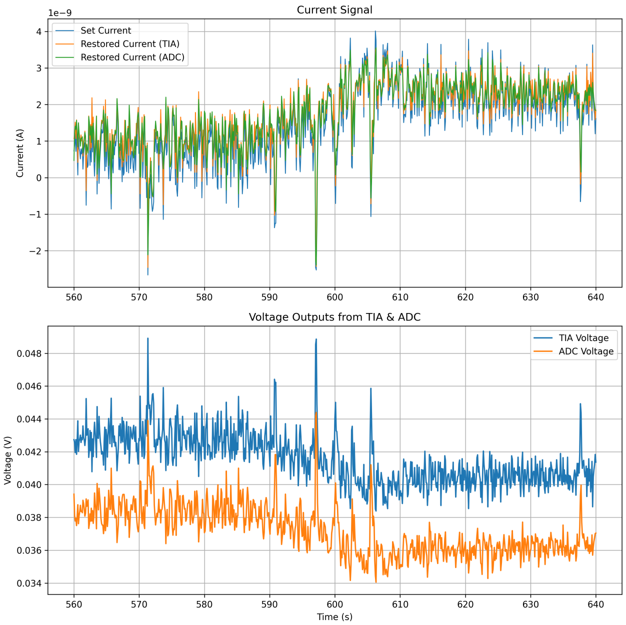

Figure 5.5: Comparison of reference input signal (hydrogen concentration data reproduced by Keithley 2470), OPA380 TIA output, and ADC output.

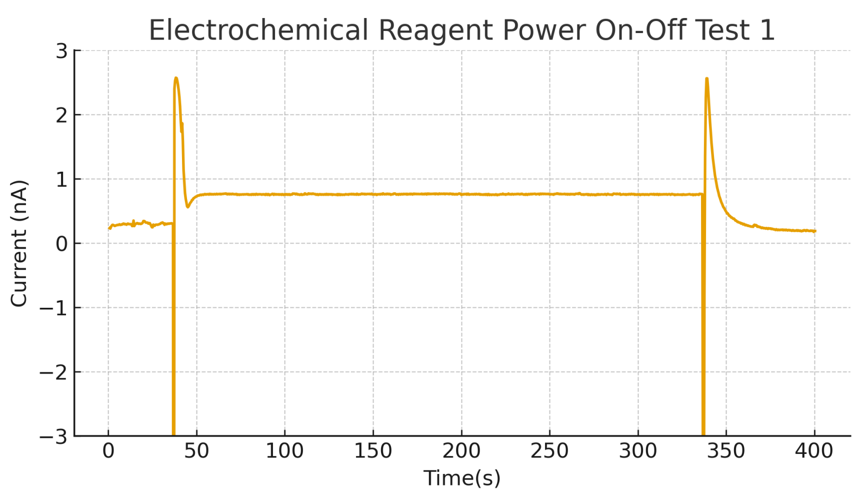

Figure 5.6: Power-up and power-down test of the ionic-liquid hydrogen Sensor.

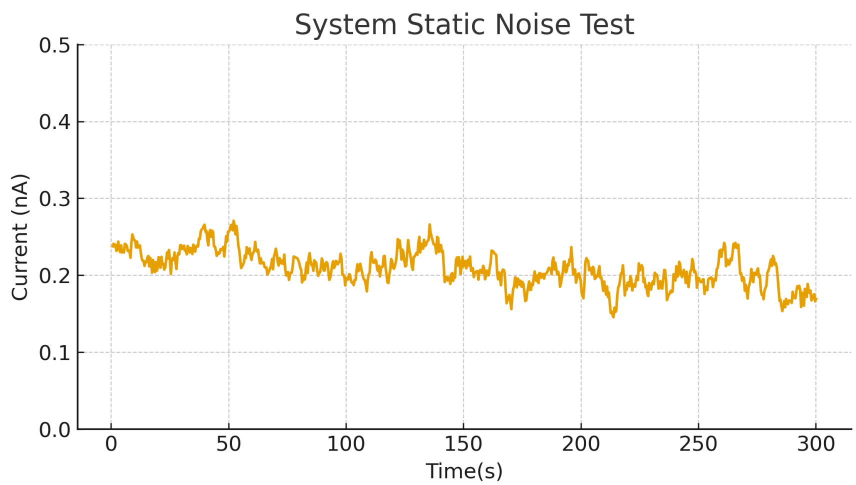

Figure 5.7: Time-domain noise of the ionic-liquid hydrogen Sensor in idle (unpowered) state.

Finally, the overall frequency-domain noise of the complete sensor-readout system was measured with the electrode chip fully connected and powered. Figure 5.8 presents the noise spectrum, highlighting the contribution of the electrode interface in addition to the readout electronics.

5.5 Summary

In this chapter, a high-sensitivity and low-noise readout system for IL H_2 sensor was experimentally validated. The system integrates a low-noise TIA (OPA380), a second-order low-pass filter, and a high-resolution ADC (ADS1262), combined with an MCU for signal processing, storage, and display.

Key findings include:

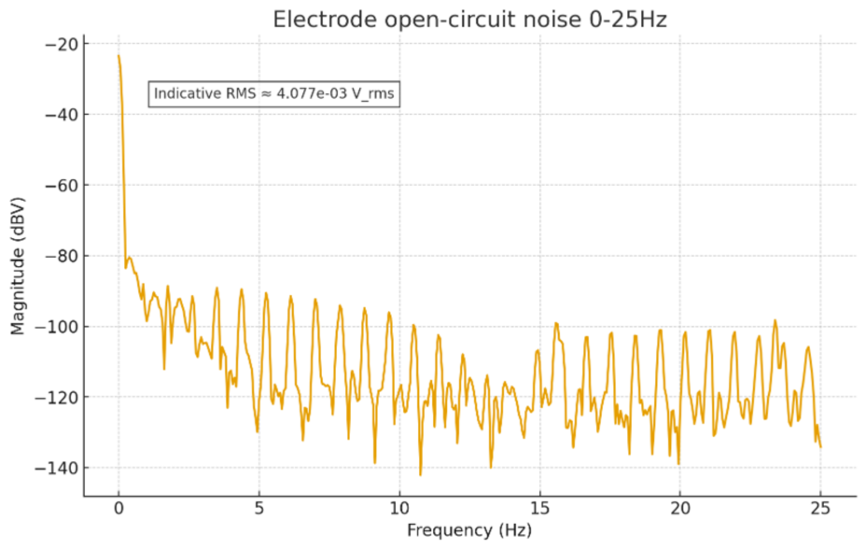

Figure 5.8: Measured frequency-domain noise of the complete electrode + readout system with ionic-liquid hydrogen sensor connected.

- **Picoampere-level sensitivity:** The readout chain exhibited linear response from 10 pA to 1 µA, with effective transimpedance gain consistent with the gigaohm feedback resistor.
- **Noise characterization:** With the electrode chip in open-circuit condition, the system noise remained within 0.1–0.3 nA, dominated by DC drift rather than high-frequency components. Frequency-domain analysis confirmed a stable background noise floor below –80 dBV above 0.2 Hz.
- **Electrode integration tests:** Power on/off experiments revealed a reproducible current difference (∼0.5 nA) when the IL H_2 sensor was biased, with baseline relaxation after shutdown.

- **System robustness:** Using the Keithley 2470 to replay real hydrogen concentration signals (collected by Prof. Xiangqun Zeng's group at the University of Missouri), the system demonstrated accurate signal processing across the full readout chain.

Overall, the experimental evaluation confirmed that the proposed design achieves stable and reproducible low-noise performance from picoampere to nanoampere currents, thereby validating its suitability for portable hydrogen detection.

CHAPTER SIX

CONCLUSION AND FUTURE WORK

6.1 Conclusion

This thesis presented the design, implementation, and validation of a portable, high-sensitivity readout interface for IL H_2 sensor. The system successfully addressed the key challenges of ultra-low current measurement, noise suppression, and integration with environmental and peripheral modules.

The major conclusions are as follows:

- The OPA380-based TIA and ADS1262 ADC achieved high-precision measurement with sub-nanoampere resolution and maintained consistency with reference Keithley SourceMeter results.

- The overall system noise floor was verified to be in the sub-nA range, with DC drift identified as the primary limitation.

- Integration of environmental monitoring (BME280), data storage, and display modules enhanced system usability, while PCB implementation demonstrated compactness and low power consumption suitable for portable operation.

- The system demonstrated robustness under both controlled current inputs and real sensor data replay, confirming its feasibility for practical hydrogen detection applications.

In conclusion, this research establishes a validated foundation for compact and low-noise hydrogen sensor readout systems, bridging the gap between laboratory-grade instruments and deployable portable platforms.

6.2 Limitations

Despite its successful implementation, the system still has certain limitations:

- The noise floor, while below 5 pA RMS, remains a challenge for measurements approaching single pA range.
- The system relies on discrete components, resulting in relatively large PCB area and power consumption ($\sim$100 mW), which could be optimized in future designs.
- Long-term stability under varying environmental conditions has not been fully characterized, especially with respect to electrode degradation and ionic liquid aging.
- The DAC-based AC excitation is currently limited in frequency range and waveform types.

6.3 Future Work

While the proposed readout system has been successfully designed and validated, several areas remain for future improvement and exploration:

- **Integration of potentiostat on PCB:** The current validation relied on an external potentiostat for electrode biasing. A fully integrated potentiostat circuit on the PCB will further reduce parasitic effects, eliminate spike noise from external instruments, and enhance the portability of the system.
- **Comprehensive noise analysis:** Although the frequency-domain noise floor was measured, more detailed analysis is required, including power spectral density (PSD), Allan deviation, and long-term drift measurements. These metrics will

enable quantitative evaluation of the limit of detection (LOD), stability, and overall sensing performance.

- **Optimization of baseline correction:** Since DC drift was identified as the dominant noise source, advanced signal processing methods or hardware-level baseline suppression techniques could be introduced to improve measurement reliability.
- **System-level validation in hydrogen chamber:** Full-scale experiments under controlled hydrogen concentrations should be conducted to directly correlate sensor current output with hydrogen levels, thereby establishing calibration curves and detection limits.
- **Broader electrochemical sensing applications:** The readout system is not limited to hydrogen detection. Its picoampere-to-nanoampere current measurement capability makes it suitable for a wide range of amperometric sensing platforms (e.g., glucose, heavy metal ions, and neurotransmitters). Future work will explore adapting the system to these applications.
- **Low-power and IoT integration:** Further optimization of firmware and hardware for ultra-low power operation will extend battery lifetime. Wireless communication modules (e.g., BLE or LoRa) could be added for real-time monitoring in IoT-based safety or environmental sensing networks.

Future work will focus on both improving the current system's performance (integration, noise, and calibration) and extending its application scope to broader electrochemical sensing fields.

REFERENCES

[1] “A review of hydrogen sensors for environmental control and life support systems,” *Applied Sciences*, vol. 13, no. 12, p. 6869, 2023.

[2] T. Hübert, L. Boon-Brett, G. Black, and U. Banach, “Hydrogen sensors—a review,” *Sensors and Actuators B: Chemical*, vol. 157, no. 2, pp. 329–352, 2011.

[3] U.S. Department of Energy, “Clean hydrogen hubs funding opportunity announcement de-foa-0002779,” Sept. 2022. Available at: `https://www.energy.gov`.

[4] “A review of hydrogen leak detection regulations and technologies,” *Energies*, vol. 17, no. 16, p. 4059, 2022.

[5] G. Korotcenkov, S.-H. Han, and J. R. Stetter, “Recent developments in hydrogen sensors based on pd-containing thin films and nanostructures: a review,” *Sensors and Actuators B: Chemical*, vol. 268, pp. 1–17, 2019.

[6] A. Ilnicka and J. P. Lukaszewicz, “Graphene-based hydrogen gas sensors: A review,” *Processes*, vol. 8, no. 5, p. 633, 2020.

[7] X. Zeng, Y. Xu, *et al.*, “Advances in electrochemical hydrogen sensing using ionic liquids: mechanisms and device integration,” *Journal of Electroanalytical Chemistry*, vol. 940, p. 117480, 2023.

[8] X. J. Liu *et al.*, “Pt/ni nanocrystal-ionic liquid interfaces for hydrogen detection,” *ACS Sensors*, 2025.

[9] A. J. Bard and L. R. Faulkner, *Electrochemical Methods: Fundamentals and Applications*. Wiley, 2 ed., 2001.

[10] Y. Xu, X. Zeng, *et al.*, “Ionic liquid-based electrochemical sensors: fundamentals, materials, and applications,” *Electrochimica Acta*, vol. 376, p. 137947, 2021.

[11] Y. Chen and H. Wang, “Low-current measurement techniques in electrochemical sensors: design of transimpedance amplifiers,” *IEEE Transactions on Instrumentation and Measurement*, vol. 69, no. 5, pp. 2130–2142, 2020.

[12] J. Li, P. Kumar, and C. Wang, “Integrated potentiostat circuits for portable electrochemical sensing: design and challenges,” *Sensors*, vol. 22, no. 12, p. 4567, 2022.

[13] F. Zhao, S. Zhou, and Y. Zhang, "Ultrasensitive detection of hydrogen peroxide using bi_2te_3 electrochemical sensors," *ACS Applied Materials & Interfaces*, vol. 13, no. 2, pp. 3089–3096, 2021.

[14] S. Woltornist, S. Panthi, and J. Zondlo, "A review of hydrogen sensing materials for safety and health applications," *Sensors*, vol. 21, no. 14, p. 4750, 2021.

[15] W. Zhang, H. Wang, and Y. Chen, "Hydrogen sensors: materials, mechanisms, and emerging technologies," *Advanced Materials*, vol. 35, no. 15, p. 2208703, 2023.

[16] H. Yin, Y. Zhang, and W. Li, "Advances in electrochemical gas sensors based on ionic liquids," *Electroanalysis*, vol. 34, no. 7, pp. 1365–1382, 2022.

[17] S. Mubeen and A. Mulchandani, "Hydrogen detection using nanostructured materials: current status and future directions," *ACS Sensors*, vol. 6, no. 3, pp. 748–767, 2021.

[18] E.-S. Lee, S.-J. Kim, and E.-S. Cho, "Nanostructured palladium and its alloys for hydrogen sensor applications: A review," *Journal of Materials Chemistry C*, vol. 8, no. 12, pp. 3974–3995, 2020.

[19] V. Kafil, B. Sreenan, M. Hadj-Nacer, Y. Wang, J. Yoon, M. Greiner, P. Chu, X. Wang, M. S. Fadali, and X. Zhu, "Review of noble metal and metal-oxide-semiconductor based chemiresistive hydrogen sensors," *Sensors and Actuators A: Physical*, 2024. https://doi.org/10.1016/j.sna.2024.115440.

[20] J. Wright *et al.*, "Real-time sensors for h subsurface storage and transportation monitoring," *DOE Hydrogen Program Review*, 2024.

[21] T. Yu *et al.*, "A robust organic hydrogen sensor for distributed monitoring," *Nature Electronics*, 2025. doi:10.1038/s41928-025-01352-y.

[22] T. Instruments, *OPA189: Zero-Drift, Ultra-Low Noise, Precision Operational Amplifier*, 2018. Datasheet, Available at: `https://www.ti.com/lit/ds/symlink/opa189.pdf`.

[23] T. Instruments, *TMUX6121: Low-Voltage Analog Switch with Low Leakage*, 2020. Datasheet, Available at: `https://www.ti.com/lit/ds/symlink/tmux6121.pdf`.

[24] T. Instruments, *DAC80502: 16-bit, Dual-Channel, Low-Noise DAC*, 2019. Datasheet, Available at: `https://www.ti.com/lit/ds/symlink/dac80502.pdf`.

[25] T. Instruments, *OPA380: High-Precision, Low-Noise, Transimpedance Amplifier*, 2017. Datasheet, Available at: `https://www.ti.com/lit/ds/symlink/opa380.pdf`.

[26] Y. Chen and H. Wang, "Low-current measurement techniques in electrochemical sensors: design of transimpedance amplifiers," *IEEE Transactions on Instrumentation and Measurement*, vol. 69, no. 5, pp. 2130–2142, 2020.

[27] D. Franks and J. Williams, "Low-noise analog filter design for precision instrumentation applications," *Analog Integrated Circuits and Signal Processing*, vol. 101, no. 3, pp. 431–442, 2019.

[28] T. Instruments, *CC2640R2F: SimpleLink Bluetooth Low Energy Wireless MCU*, 2019. Datasheet, Available at: `https://www.ti.com/lit/ds/symlink/cc2640r2f.pdf`.

[29] T. Instruments, *ADS1262: 32-bit, Low-Noise, Delta-Sigma ADC with Integrated PGA*, 2018. Datasheet, Available at: `https://www.ti.com/lit/ds/symlink/ads1262.pdf`.

[30] T. Instruments, *MSP430F6736A: 24-bit Sigma-Delta ADC Integrated Ultra-Low Power MCU*, 2020. Datasheet, Available at: `https://www.ti.com/lit/ds/symlink/msp430f6736a.pdf`.

[31] B. Sensortec, *BME280: Combined Humidity and Pressure Sensor*, 2018. Datasheet, Available at: `https://www.bosch-sensortec.com/products/environmental-sensors/humidity-sensors-bme280/`.

[32] B. Sensortec, *BMP280: Digital Pressure Sensor*, 2016. Datasheet, Available at: `https://www.bosch-sensortec.com/products/environmental-sensors/pressure-sensors/bmp280/`.

[33] Sensirion, *SHT31: Humidity and Temperature Sensor*, 2019. Datasheet, Available at: `https://www.sensirion.com/sht3x`.

[34] T. Connectivity, *HTU21D: Digital Relative Humidity Sensor*, 2014. Datasheet, Available at: `https://www.te.com/usa-en/product-CAT-HSC0004.html`.

[35] J. Wang and H. Sun, "Environmental monitoring integration in portable electrochemical sensors: design considerations and challenges," *Sensors and Actuators B: Chemical*, vol. 301, p. 127061, 2019.

[36] T. Instruments, *BQ24074: Li-Ion Battery Charger with Power Path Management*, 2018. Datasheet, Available at: `https://www.ti.com/lit/ds/symlink/bq24074.pdf`.

[37] T. Instruments, *TPS61022: High Efficiency 2A Boost Converter*, 2019. Datasheet, Available at: `https://www.ti.com/lit/ds/symlink/tps61022.pdf`.

[38] T. Instruments, *TPS7A4700: Ultralow-Noise, High-PSRR, Low-Dropout Linear Regulator*, 2017. Datasheet, Available at: `https://www.ti.com/lit/ds/symlink/tps7a4700.pdf`.

[39] W. Zhang and C. Liu, "Low-noise power management techniques for precision analog front-end systems," *IEEE Transactions on Power Electronics*, vol. 35, no. 12, pp. 13245–13256, 2020.

[40] S. Association, *SD Specifications Part 1: Physical Layer Simplified Specification*, 2018. Available at: `https://www.sdcard.org`.

[41] S. Systech, *SSD1306: 128×64 Dot Matrix OLED/PLED Segment/Common Driver*, 2015. Datasheet, Available at: `http://www.solomon-systech.com`.